Electronic Supplementary Material (ESI) for Journal of Materials Chemistry A.
This journal is © The Royal Society of Chemistry 2019

Supporting Information

Boron and Nitrogen Co-Doped Porous Carbon Nanofibers as Metal-free Catalysts for Highly Efficient Ammonia Electrosynthesis

Yan Kong,[a] Yan Li,[a] Bin Yang,[a] Zhongjian Li,[a] Yao Yao,[b] Jianguo Lu,[d] Lecheng Lei,[a] Zhenhai Wen,[c] Minhua Shao,[b,*] Yang Hou[a,*]

[a] Key Laboratory of Biomass Chemical Engineering of Ministry of Education, College of Chemical and Biological Engineering, Zhejiang University, Hangzhou, 310027, China

[b] Department of Chemical and Biological Engineering, The Hong Kong University of Science and Technology, Clear Water Bay, Kowloon, Hong Kong, China

[c] CAS Key Laboratory of Design and Assembly of Functional Nanostructures, and Fujian Provincial Key Laboratory of Nanomaterials, Fujian Institute of Research on the Structure of Matter, Chinese Academy of Sciences, Fuzhou, Fujian 350002, China

[d] State Key Laboratory of Silicon Materials, School of Materials Science and Engineering, Zhejiang University, Hangzhou, 310027, China

* E-mail: yhou@zju.edu.cn; kemshao@ust.hk

Experimental section

Preparation of B/N-CNF

Boric acid and polyacrylonitrile (PAN) were mixed in 25 mL of N, N-dimethyl formamide (DMF) at 25 ^{o}C to form uniform solution after continuous mechanical stirring for 4 h. Then, the solution was loaded into plastic syringe with needle (a diameter of 0.5 mm) and the electrospinning was conducted at 25 kV with an injecting rate of 0.6 mL h^{-1}. The collector was a rolling Al foil roller with a distance of 20 cm to the mental needle. The as-spun PAN CNF with boric acid was firstly stabilized at 250 ^{o}C for 2 h in air atmosphere at a heating rate of 3 ^{o}C min^{-1}. Next, the intermediate was carbonized in NH_3 atmosphere for 2 h at the temperatures (700 ^{o}C, 800 ^{o}C, 900 ^{o}C, and 1000 ^{o}C) at a heating rate of 3 ^{o}C min^{-1}.

Preparation of B-CNF

Boric acid and PAN were mixed in 25 mL DMF at 25 ^{o}C to form uniform solution after continuous mechanical stirring for 4 h. Then, the solution was loaded into plastic syringe with needle (a diameter of 0.5 mm) and the electrospinning was conducted at 25 kV with an injecting rate of 0.6 mL h^{-1}. The collector was a rolling aluminum foil roller with a distance of 20 cm to the mental needle. The as-spun PAN CNF with boric acid was firstly stabilized at 250 ^{o}C for 2 h in air atmosphere at a heating rate of 3 ^{o}C min^{-1}. Next, the intermediate was carbonized in N_2 atmosphere for 2 h at 900 ^{o}C with a heating rate of 3 ^{o}C min^{-1}.

Preparation of N-CNF

PAN was mixed in 25 mL of DMF at 25 ^{o}C to form uniform solution after continuous mechanical stirring for 4 h. Then, the solution was loaded into plastic syringe with needle (a diameter of 0.5 mm) and the electrospinning was conducted at 25 kV with an injecting rate of 0.6 mL h^{-1}. The collector was a rolling aluminum foil roller with a distance of 20 cm to the mental needle. The as-spun PAN CNF was firstly stabilized at 250 ^{o}C for 2 h in air atmosphere at a heating rate of 3 ^{o}C min^{-1}. Next, the intermediate was carbonized in NH_3 atmosphere for 2 h at 900 ^{o}C with a heating rate of 3 ^{o}C min^{-1}.

Characterization

The morphology of sample was measured with field-emission scanning electron microscope (FESEM, SU-8010), transmission electron microscopy (TEM, HT7700), and high-resolution TEM (HRTEM, JEM-2100). X-ray diffraction (XRD) patterns were investigated with Cu Kα radiation by LabX XRD-6000. Raman tests were conducted on a LabRAM HR Evolution Raman Microspectroscopy with a laser of 532 nm. The element composition of samples was characterized by X-ray photoelectron spectroscopy (XPS) on Escalab 250Xi X-ray photoelectron spectroscopy using Al Kα radiation. The porous structure and surface area were measured by Brunauer–Emmett–Teller (BET, Micromeritics ASAP 2020) measurement. The FTIR spectra were conducted with Nicolet 5700, ThermoFisher.

Electrochemical measurements

The NRR activity was measured by electrochemical station (CHI 760E) with a two-compartment cell at room temperature, which was separated by a Nafion 211 membrane. For the three-electrode system, a platinum (Pt) foil and a saturated Ag/AgCl were acted as the counter electrode and reference electrode, respectively. The working electrode was prepared as follows. 10 mg of catalyst was dispersed into the mixture solution (900 μL ethyl alcohol and 100 μL 5 wt.% Nafion solution) by sonication for at least 2 h to produce a uniform ink. Then, 100 μL of ink was carried onto a piece of carbon paper with an area of 1 x 1 cm^2, followed by drying at 25 ^oC. All potentials were calibrated to RHE with the equation: E (RHE) = E (Ag/AgCl) + 0.059 × pH + 0.197 (V). For NRR process, the B/N-CNFs was deposited on the carbon paper as cathodic electrode, the NRR worked under room temperature and atmosphere pressure. During the reaction process, the protons (H^+ ions) will transport through the electrolyte (0.1 M KOH solution), then react with N_2 to fabricate NH_3, with N_2 incessantly bubbled into the cathodic compartment.

Linear sweep voltammetry (LSV) was carried at the scan rate of 5 mV s^{-1} after cyclic voltammetry (CV) cycles with a scan rate of 50 mV s^{-1}. Tafel slope was figured out according to the above LSV curve, and electrochemical impedance spectroscopy (EIS) was investigated at potential of 1.55 V. Besides, the electrochemical double layer capacitance was calculated by the CV cycles at the different scan rates from 100

mV to 20 mV. The NRR activity was obtained by potentiostatic test in N_2 saturated 0.1 M KOH solution (25 mL) after the electrolyte was aerated with N_2 for 0.5 h. The potentiostatic test was also carried out in Ar-saturated cathodic compartment for comparison.

Determination of NH_3

The NH_3 presented in the electrolyte was spectrophotometrically measured by the indophenol blue method. Firstly, 2 mL of electrolyte after NRR process was dispersed into 2 mL of mixture solution consisting of sodium hydroxide solution (1.0 M), salicylic acid (5 wt.%), and sodium citrate (5 wt.%), followed by addition of 1 mL of 0.05 M NaClO and 0.2 mL of 1 wt.% $C_5FeN_6Na_2O$. Then, UV-Vis absorption spectrum was collected after keeping 2 h at room temperature. At the wavelength of 665 nm, the formed indophenol blue was determined, and the concentration-absorbance curves were calibrated using standard NH_4Cl solution with a series of concentrations (0.05 ~ 3.0 μg mL^{-1}), which contained the same concentration of KOH solution used in the electrocatalysis process. The fitting curve ($y = 0.409x - 0.013$, $R^2 = 0.999$) displayed good linear relation of absorbance value with NH_4Cl concentration by three times independent calibrations.

Determination of N_2H_4

The concentration of N_2H_4 was determined by the Watt and Chrisp method. In detail, 5 mL of electrolyte after NRR reaction was added into the color reagent (5.99 g of para-(dimethylamino) benzaldehyde dissolved in a mixture of 30 mL of concentrated HCl and 300 mL of ethanol). After stirring the mixed solution for 10 min at room temperature, the absorbance was measured at 458 nm, and the N_2H_4 yields were estimated from a standard curve. The calibration curve demonstrated good linear relation of absorbance with N_2H_4 concentration ($y = 0.565x + 0.017$, $R^2 = 0.999$) by three times independent calibrations.

Determination of Nitrate

Nitrates show typical absorption to UV light at the wavelength of 220 nm, in which the absorbance value is in direct proportion to the concentration of nitrates. Therefore, the content of the NO_3^- can be quantitatively determined by ultraviolet spectroscopy.

In a typical procedure, 5.0 mL of standard solutions or sample electrolytes were added to the bottle followed by addition of 0.10 mL of 1.0 M HCl solution. After shaking up and standing for 5 min, the concentration of nitrate was measured using UV-vis spectrophotometer at wavelength range from 200 nm to 300 nm. The standard curve NO_3^- determination was then plotted with the absorbance value difference at 220 nm and 275 nm as y axis and the concentration of NO_3^- as x axis. The calibration curve demonstrated good linear relation of absorbance with NO_3^-concentration ($y = 0.0469x - 0.0001$, $R^2 = 0.9991$) by three times independent calibrations.

Determination of Nitrite

Nitrites can be diazotized by sulfanilamide under acid environment, and the diazotized compound can be coupled with N-(1-Naphthyl) ethylenediamine dihydrochloride, producing pink azo dyes which show typical absorption at wavelength of 540 nm. Therefore, the content of the nitrite can be quantitatively determined using diazo coupling spectroscopy. In a typical procedure, 5.0 mL of standard solutions or sample electrolytes were added to the bottles, followed by addition of 0.10 mL of 2 M HCl solution with 10 mg mL^{-1} sulfanilamide. After shaking up and standing for 5 min, 0.10 mL of 1 mg mL^{-1} N-(1-Naphthyl) ethylenediamine dihydrochloride solution was added to the above solution. The solution was then shaken up and allowed to stand for 30 min, and the concentration of NO_2^- was measured using UV-vis spectrophotometer at wavelength range from 450 nm to 650 nm. The standard curve for NO_2^- determination was then plotted with the absorbance value difference at 540 nm and 650 nm as y axis and the concentration of NO_2^- as x axis. The calibration curve demonstrated good linear relation of absorbance with NO_3^-concentration ($y = 0.0012x + 0.0118$, $R^2 = 0.9991$) by three times independent calibrations.

^{15}N isotope labeling experiment

The isotopic labeling experiment was carried out using $^{15}N_2$ as the feeding gas (98 atom % ^{15}N) with 0.1 M KOH electrolyte. After electrocatalysis at −0.5 V vs. RHE for 2 h, 0.5 M H_2SO_4 was added to the electrolyte to acidized to PH ~3, and then concentrated to 2 mL by evaporating at 70 ^oC. Afterwards, 0.9 mL of the resulting

solution was taken out and mixed with 0.1 mL D_2O containing 100 ppm dimethyl sulphoxide as an internal standard for ^1H nuclear magnetic resonance measurement (^1H NMR, Bruker Avance III 400 MHz).

Determination of FE and NH_3 yield rate

The total amount of NH_3 produced was measured using colorimetric methods. Assuming three electrons were needed to produce one NH_3 molecule, the Faradaic efficiency could be calculated as follows:

$$\text{Faradaic efficiency} = 3\ F \times (c(NH_3) \times V)/Q$$

where F is the Faraday constant, Q is the charge accumulated via 2 h electrocatalysis, and V is the volume of the KOH electrolyte.

The ammonia yield rate was calculated using the following equation:

$$\text{Ammonia yield rate} = (c(NH_3) \times V)/(t \times m)$$

where $c(NH_3)$ is the concentration of measured NH_3, V is the volume of the KOH electrolyte, t is the reduction reaction time and m is the loading mass of catalysts.

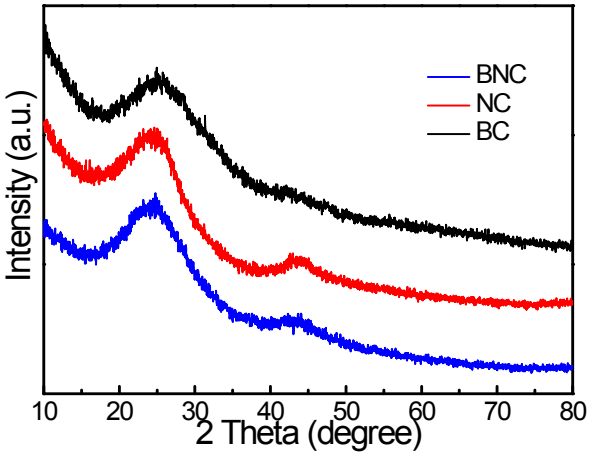

Figure S1. XRD patterns of B/N-CNF, N-CNF, and B-CNF.

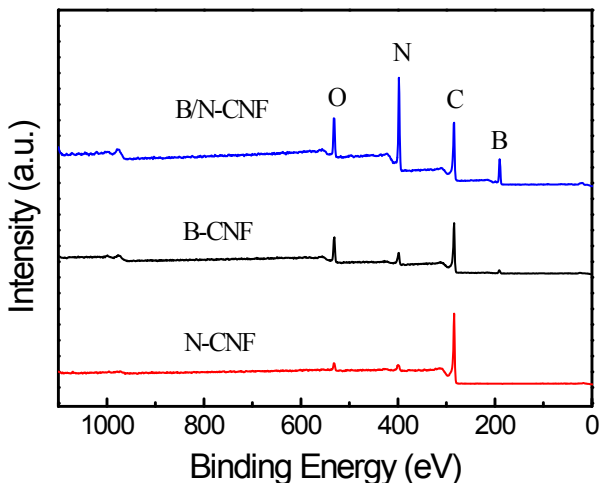

Figure S2. XPS survey spectra of B/N-CNF, N-CNF, and B-CNF.

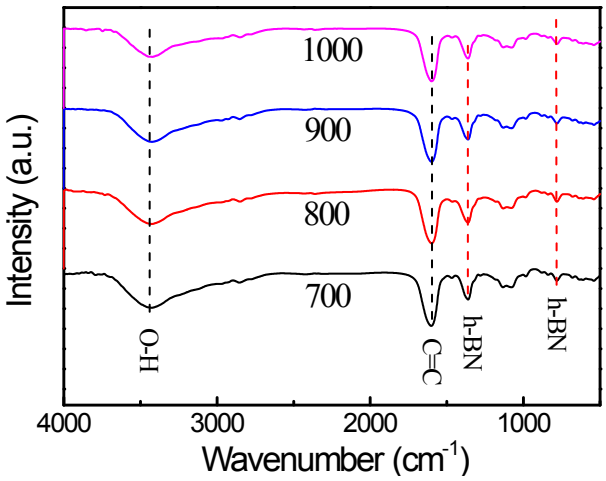

Figure S3. FTIR spectra of B/N-CNF-700, B/N-CNF-800, B/N-CNF, and B/N-CNF-1000.

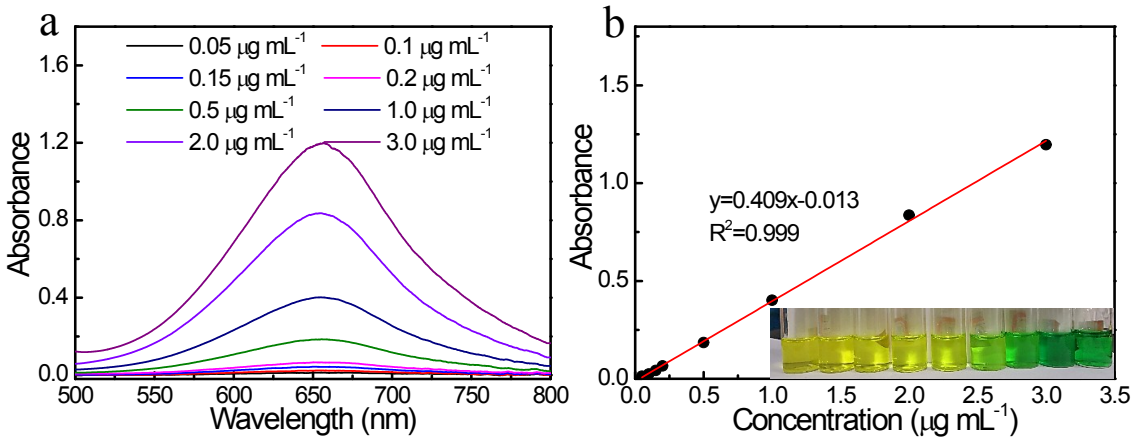

Figure S4. (a) UV-Vis absorption spectra of various NH_4^+ concentrations (0.05 ~ 3.0 μg mL^{-1}) after reacting with indophenol blue reagent for 2 h at room temperature. (b) The corresponding calibration curve used to determine NH_4^+ concentrations.

Calibration curve for colorimetric NH_3 assay in 0.1 M KOH reacted with the indophenols blue method. The absorbance at 665 nm was measured and the fitting curve showed a good linear relation of absorbance with NH_4^+ ion concentration (y = 0.409x - 0.013, R^2 = 0.999) of three times independent calibration curves. The determination of NH_3 concentration in 0.1 M KOH during electrochemical tests was performed by this equation.

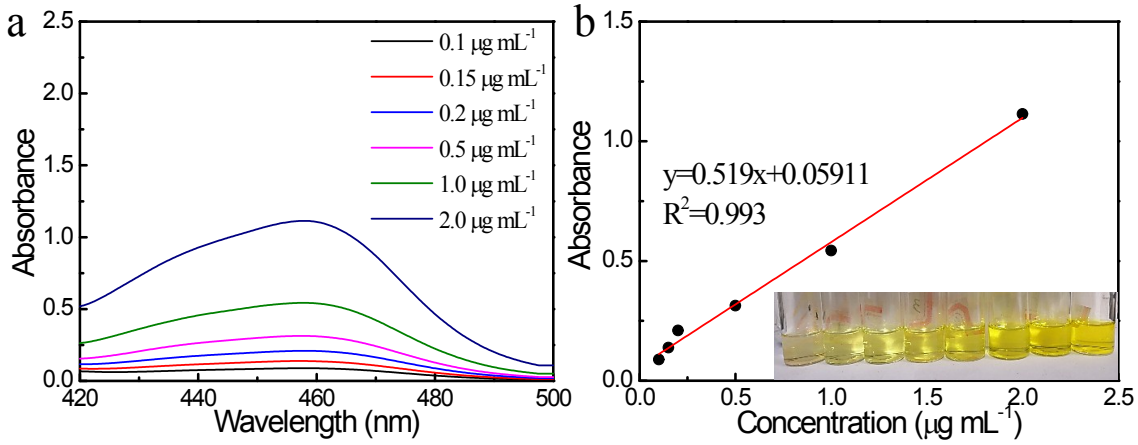

Figure S5. (a) UV-Vis absorption spectra of various N_2H_4 concentrations (0.1 ~ 2.0 μg mL^{-1}) using the Watt and Chrisp method at room temperature. (b) The corresponding calibration curve used to determine N_2H_4 concentrations.

Calibration curve for colorimetric N_2H_4 assay in 0.1 M KOH reacted with the Watt and Chrisp method. The absorbance at 458 nm was measured and the fitting curve shows a good linear relation of absorbance with N_2H_4 concentration ($y = 0.519x + 0.059$, $R^2 = 0.993$) of three times independent calibration curves.

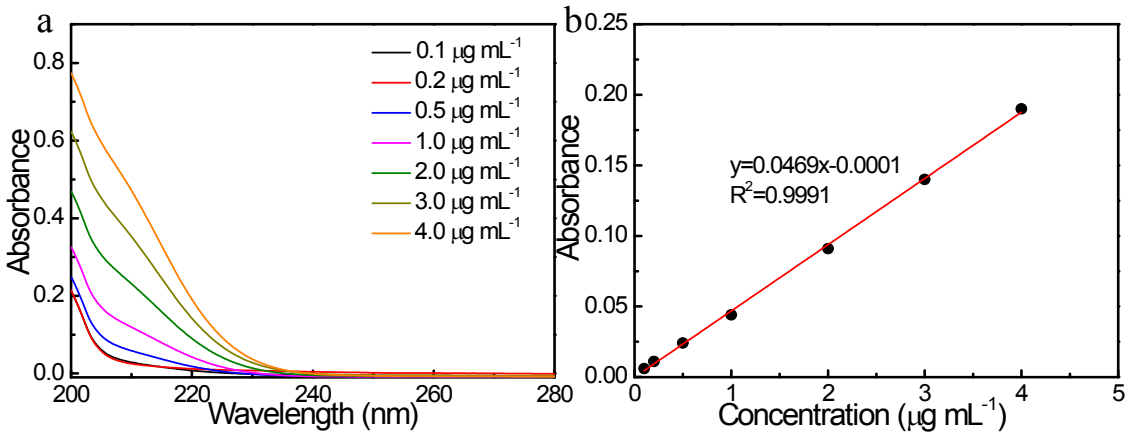

Figure S6. (a) UV-Vis absorption spectra of various KNO_3 concentrations (0.1 ~ 4.0 μg mL^{-1}). (b) The corresponding calibration curve used to determine nitrate concentrations.

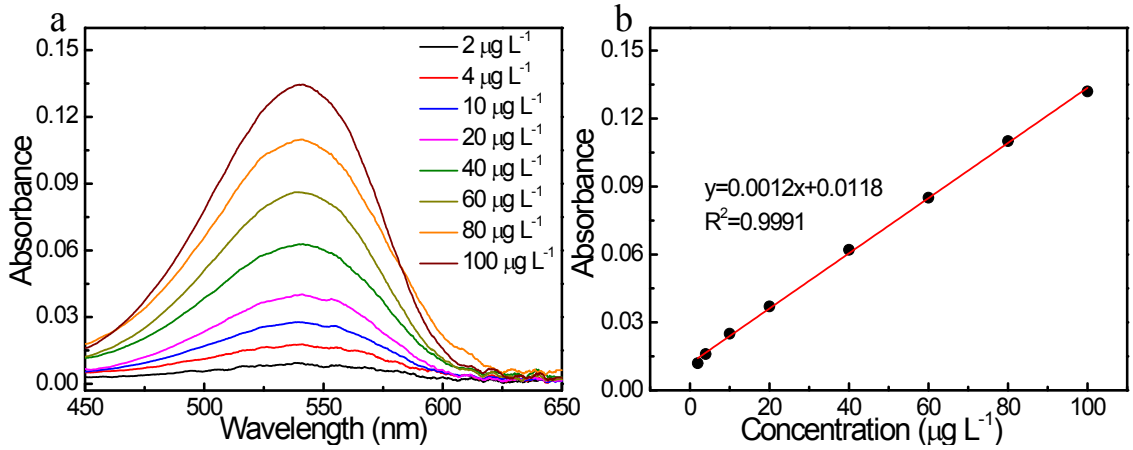

Figure S7. (a) UV-Vis absorption spectra of various KNO_2 concentrations (2 ~ 100 μg L^{-1}). (b) The corresponding calibration curve used to determine nitrite concentrations.

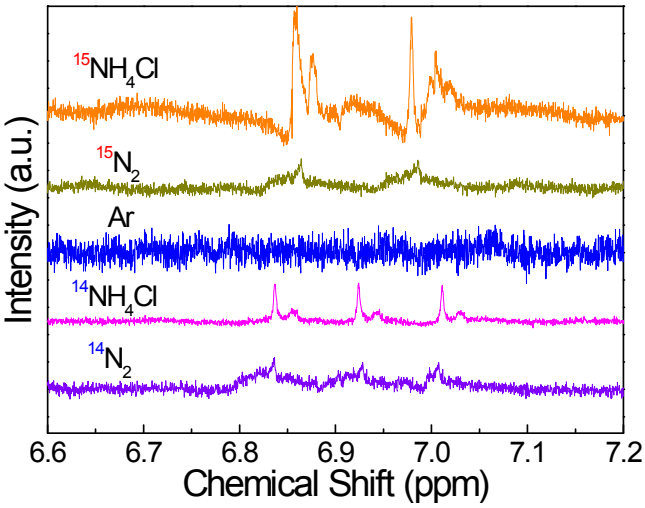

Figure S8. Isotopic labeling results of both $^{14}NH_4^+$and $^{15}NH_4^+$ obtained from the NRR reaction at -0.5 V using $^{14}N_2$ or $^{15}N_2$ as the nitrogen source, respectively.

The corresponding ^1H NMR spectra had only a double peak of $^{15}NH_4^+$, which confirmed that the formation of NH_3 was completely derived from the electrochemical reduction of N_2 in the presence of B/N-CNF. Besides, only $^{14}NH_4^+$ was detected from electrochemical NRR when using $^{14}N_2$ as the feeding gas, as well. Also, no any peaks about $^{14}NH_4^+$ or $^{15}NH_4^+$ under Ar atmosphere were observed. These results clearly demonstrated that the B/N-CNF can efficiently transfer N_2 into NH_3 via electrochemical NRR.

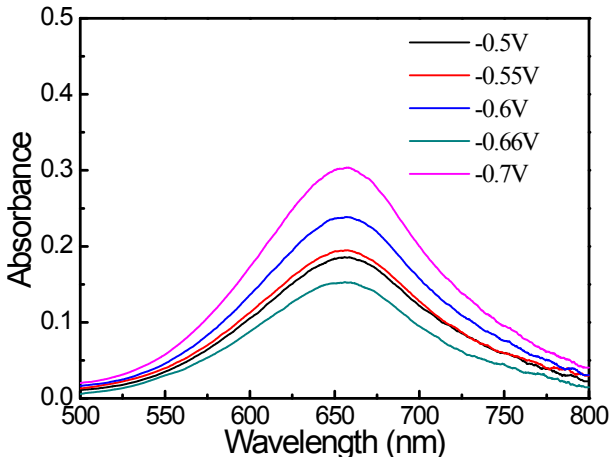

Figure S9. UV-Vis absorption spectra of the electrolytes stained with indophenol indicator after NRR electrocatalysis on the B/N-CNF electrode at the potentials from -0.50 ~ -0.70 V for 2 h for NH_3 determination.

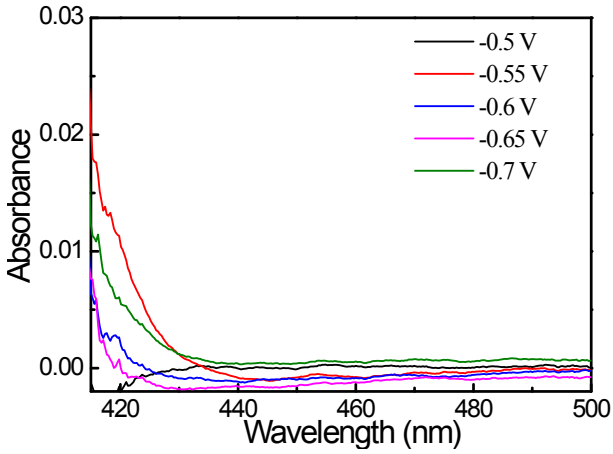

Figure S10. UV-Vis absorption spectra of the electrolytes after NRR electrocatalysis on the B/N-CNF electrode at the potentials from -0.50 ~ -0.70 V for 2 h for N_2H_4 determination.

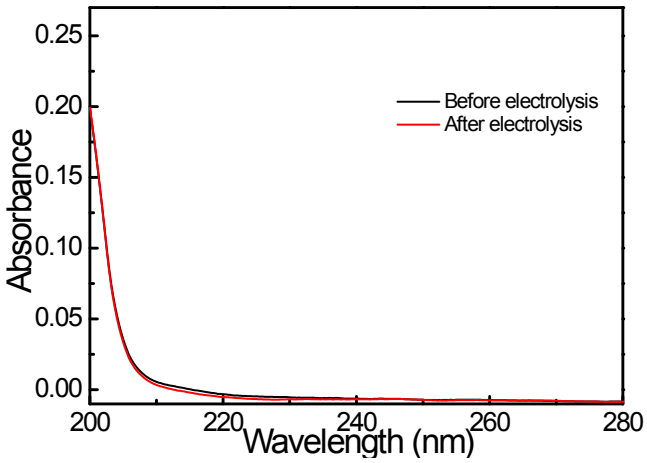

Figure S11. UV-Vis absorption spectra of the electrolytes before and after NRR electrocatalysis on the B/N-CNF electrode for NO_3^- determination.

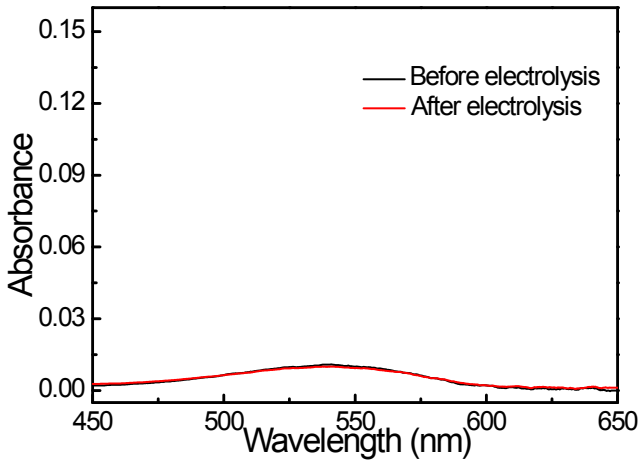

Figure S12. UV-Vis absorption spectra of the electrolytes after NRR electrocatalysis on the B/N-CNF electrode for NO_2^- determination.

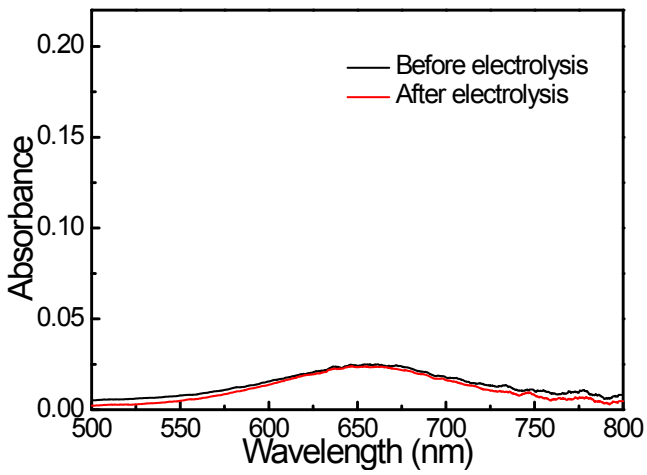

Figure S13. UV-Vis absorption spectra of the electrolytes stained with indophenol indicator before and after continuously feeding N_2 for 2 h under ambient condition.

With continuously feeding N_2 under ambient condition, the UV-Vis absorption spectra of the electrolytes stained with indophenol indicator before and after 2h were not obviously changed, confirming that the ambient ammonia did not contribute to the ammonia productions.

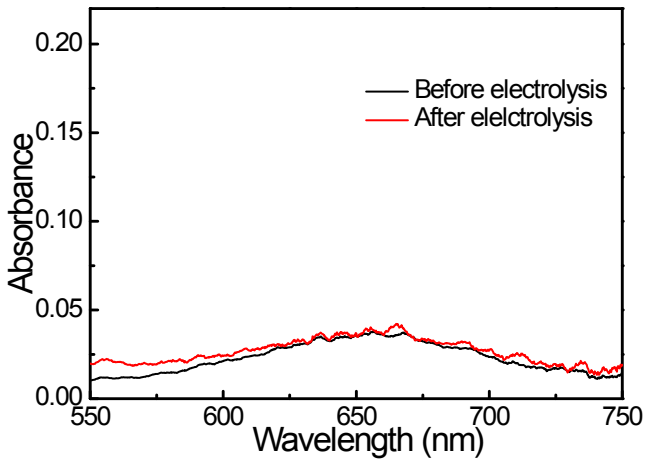

Figure S14. UV-Vis absorption spectra of the electrolytes stained with indophenol indicator continuously feeding N_2 gas before and after 2 h NRR electrocatalysis on the B/N-CNF electrode at open-circuit potential under ambient condition.

At open-circuit potential under ambient condition, the UV-Vis absorption spectra of the electrolytes stained with indophenol indicator before and after NRR electrocatalysis were not obviously changed, confirming that the ambient ammonia did not contributed to the NH_3 productions.

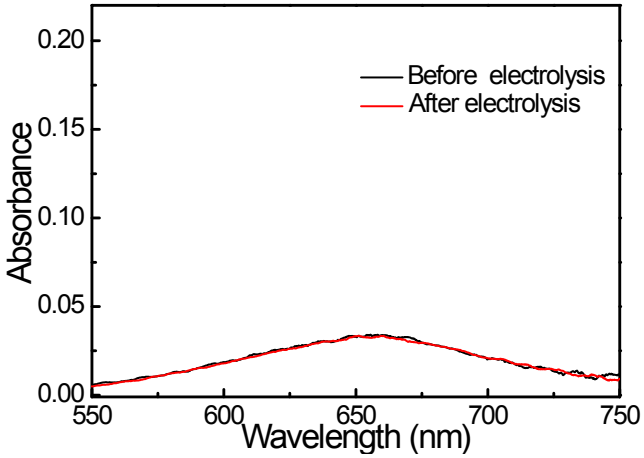

Figure S15. UV-Vis absorption spectra of the electrolytes stained with indophenol indicator before and after continuously supplying N_2 gas for 2 h on the bare carbon paper electrode at the potential of -0.5 V.

Carbon paper as the working electrode at -0.5 V with continuously supplying N_2 were used for electrochemical NRR. No difference of the UV-Vis absorption spectra of the electrolytes was found before and after NRR electrocatalysis, revealing that the high NRR performance are attributed to the B/N-CNF catalyst instead of carbon paper supports.

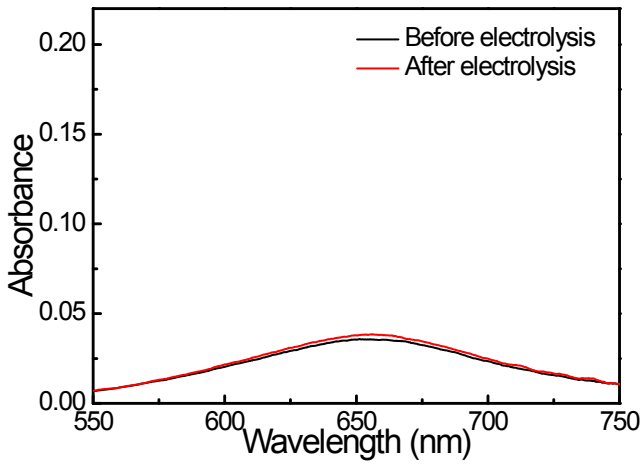

Figure S16. UV-Vis absorption spectra of the electrolytes stained with indophenol indicator before and after 2 h electrocatalysis on the B/N-CNF electrode at the potential of -0.5 V in Ar atmosphere.

With continuously supplying Ar gas, the UV-Vis absorption spectra of the electrolytes after electrocatalysis at -0.5 V was in accordance with that of before electrocatalysis, demostrating that no additional NH_3 gas are produced without N_2 sources in this system.

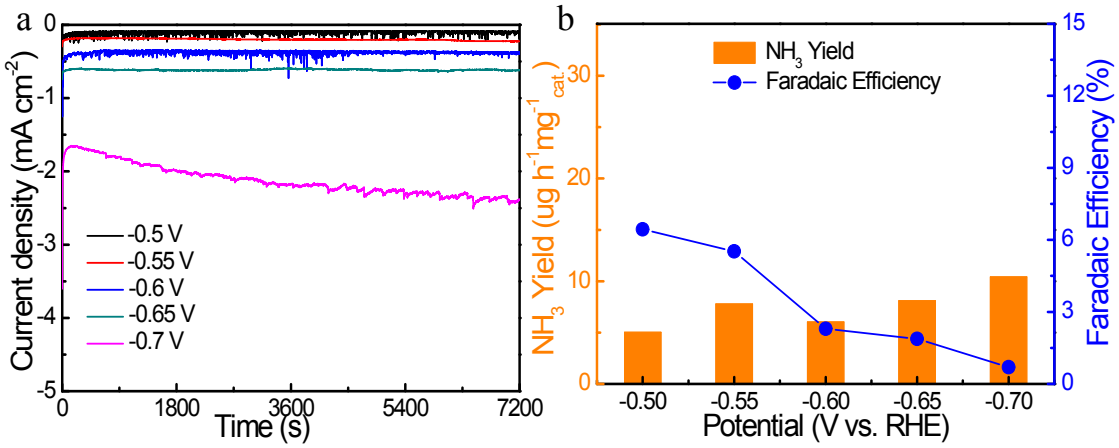

Figure S17. (a) Chronoamperometric curves of B/N-CNF at different applied potentials in 0.1 M HCl electrolyte. (b) NH_3 yields (yellow) and FE values (blue) of B/N-CNF at different applied potentials.

In acid electrolyte, the FEs and NH_3 yields of B/N-CNF at different applied potentials were showed in Figure S17, where the highest FE value of 6.44% at -0.5 V associated with NH_3 yield of 10.42 μg h^{-1} $mg^{-1}_{cat.}$ at -0.7 V were obtained for the B/N-CNF. With the further decreasing applied potential, the FE values were gradually decreased due to the competitive HER.

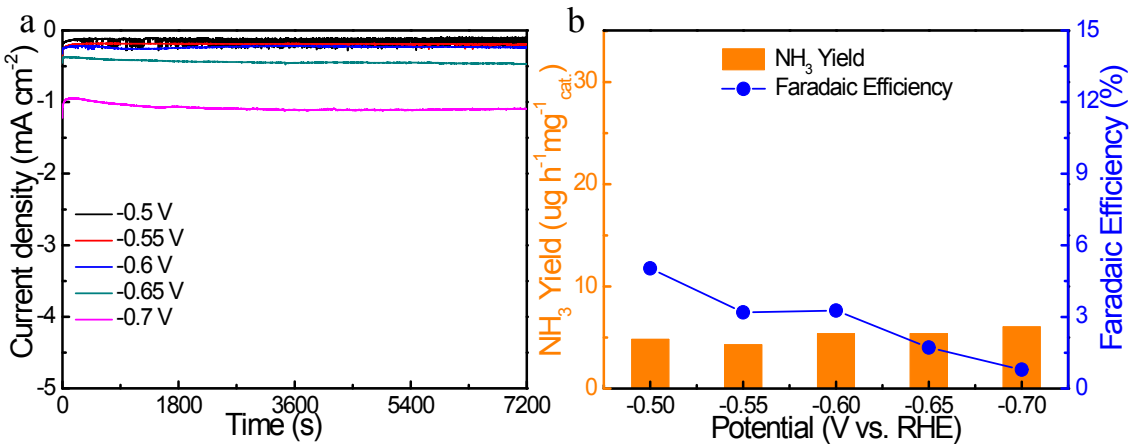

Figure S18. (a) Chronoamperometric curves of B/N-CNF at different applied potentials in 0.1 M Na_2SO_4 electrolyte. (b) NH_3 yields (yellow) and FE values (blue) of B/N-CNF at different applied potentials.

In neutral electrolyte, the FEs and NH_3 yields of B/N-CNF at different applied potentials were showed in Figure S18, where the highest FE value of 5.03% at -0.5 V associated with NH_3 yield of 6.04 μg h^{-1} $mg^{-1}_{cat.}$ at -0.7 V were obtained for the B/N-CNF. With the further decreasing applied potential, the FE values were gradually decreased.

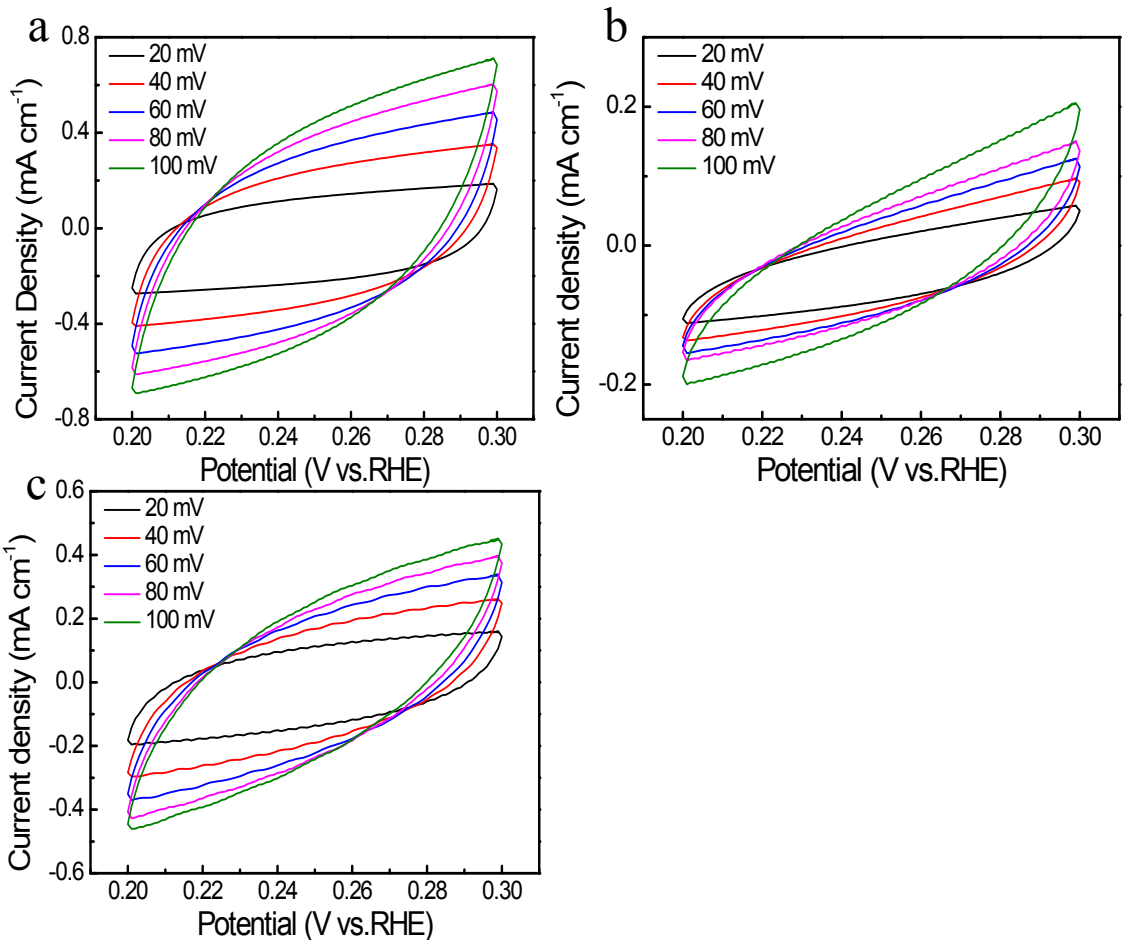

Figure S19. CV curves of (a) B/N-CNF, (b) N-CNF and (c) B-CNF at various scan rates (20 to 100 mV s^{-1}) in the range of 0.30 to 0.20 V.

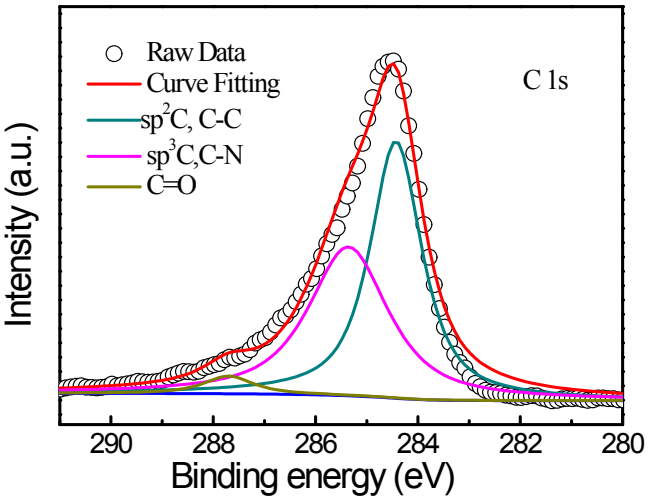

Figure S20. The high-revolution C 1s XPS spectra of B/N-CNF.

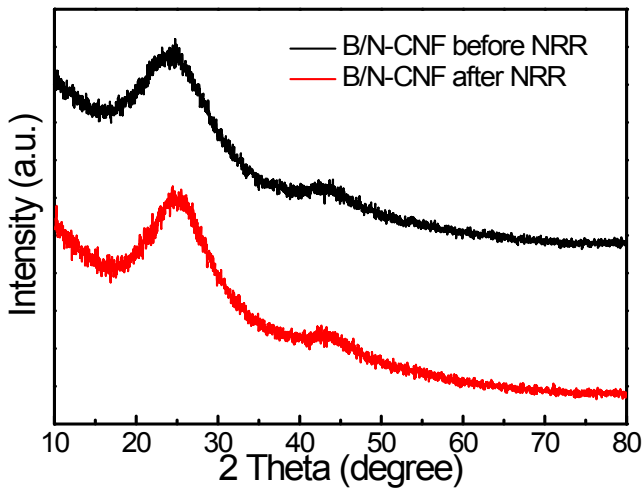

Figure S21. XRD patterns of B/N-CNF before and after NRR.

The XRD pattern of B/N-CNF after NRR electrocatalysis showed two obvious peaks located at 26° and 44°, which indicated that B/N-CNF still retained the initial crystalline state.

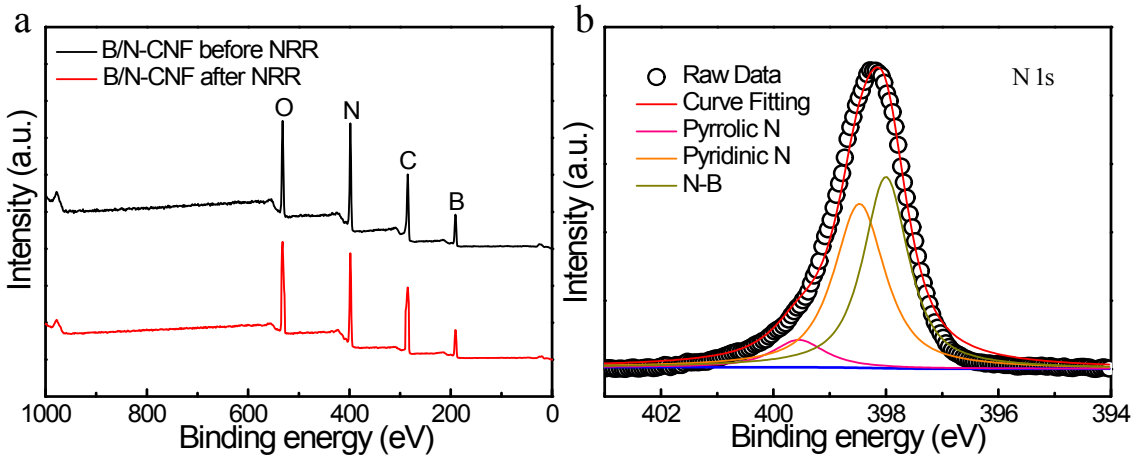

Figure S22. (a) XPS survey spectra of B/N-CNF before and after NRR electrocatalysis. (b) High-resolution N 1s XPS spectra of B/N-CNF after NRR electrocatalysis.

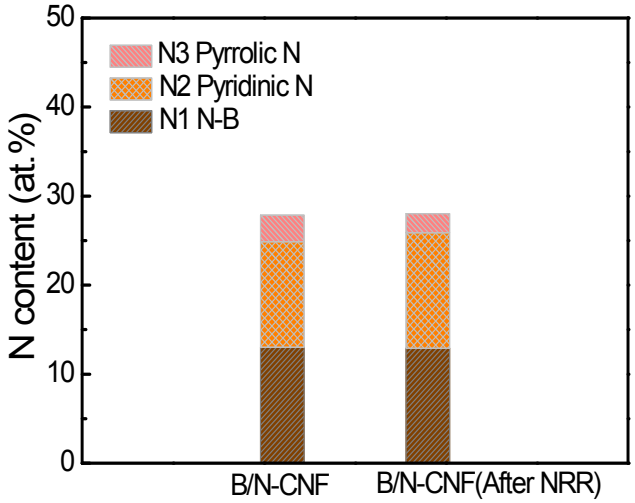

Figure S23. The contents of different N species of B/N-CNF after NRR electrocatalysis.

After electrochemical NRR process, the content of N element was in accordance with the B/N-CNF without NRR electrocatalysis, and the N species consisting of 12.9% of B-N (N1, 397.8 eV), 13.0% of pyridinic N (N2, 398.4 eV), and 2.1% pyrrolic N (N3, 399.5 eV), remained initial compositions approximately. Therefore, the above results further confirmed the stability of B/N-CNF catalysts. The revisions can be found in the revised manuscript on Page S22.

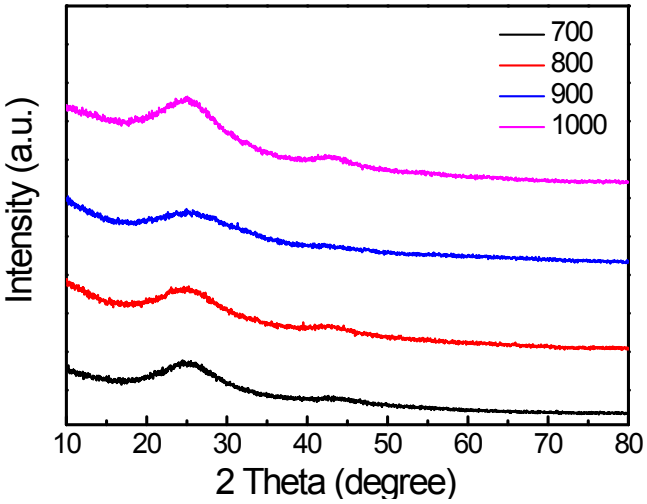

Figure S24. XRD patterns of B/N-CNF-700, B/N-CNF-800, B/N-CNF, and B/N-CNF-1000.

As shown in Fig. S10, XRD patterns of B/N-CNFs with different calcination temperatures still possessed two obvious peaks at 26° and 44 °, which are indexed to (002) and (100) planes of the carbon phase, respectively.

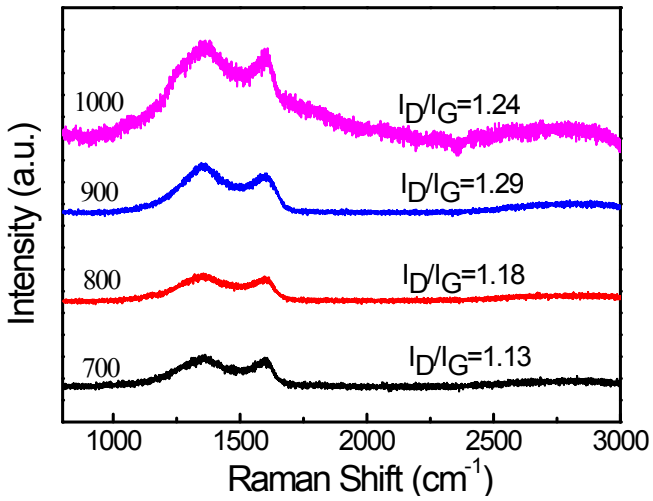

Figure S25. Raman spectra of B/N-CNF-700, B/N-CNF-800, B/N-CNF, and B/N-CNF-1000.

The I_D/I_G results clearly displayed that the B/N-CNF possessed more defective sites than the B/N-CNF-1000, B/N-CNF-800, and B/N-CNF-700.

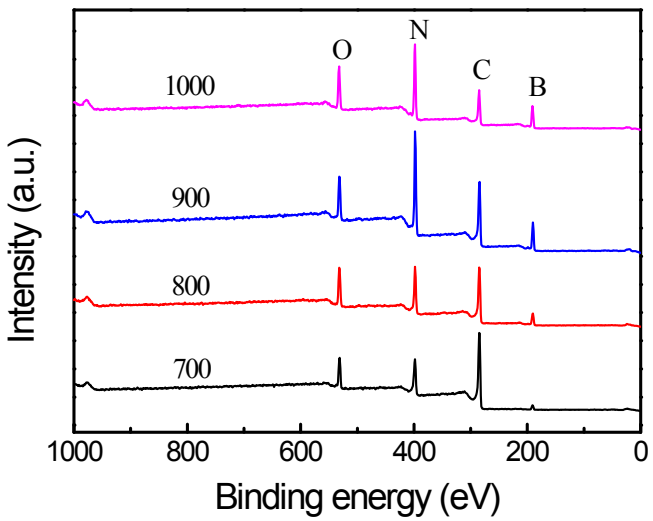

Figure S26. XPS survey spectra of B/N-CNF-700, B/N-CNF-800, B/N-CNF, and B/N-CNF-1000.

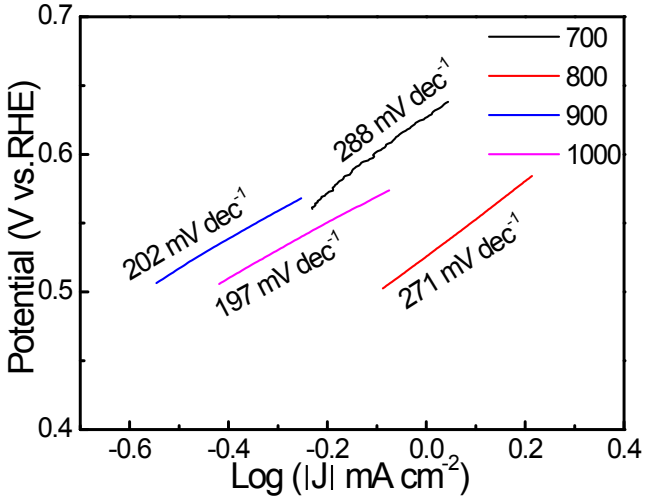

Figure S27. The Tafel slopes of B/N-CNF-700, B/N-CNF-800, B/N-CNF, and B/N-CNF-1000.

As shown in Fig. S13, the Tafel slopes of B/N-CNF-1000, B/N-CNF-800, and B/N-CNF-700 were 197 mV dec^{-1}, 271 mV dec^{-1}, and 288 mV dec^{-1}, respectively.

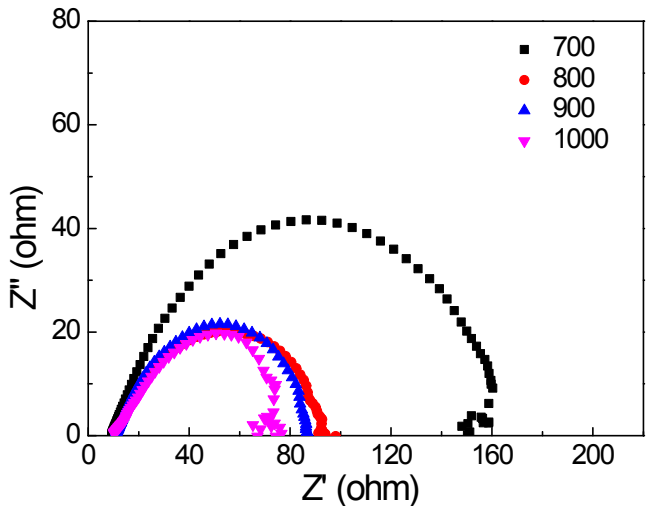

Figure S28. EIS spectra of B/N-CNF-700, B/N-CNF-800, B/N-CNF, and B/N-CNF-1,000.

As shown in Fig. S14, no obvious difference in charge-transfer resistance was observed for B/N-CNF-800, B/N-CNF, and B/N-CNF-1000, but the B/N-CNF-700 exhibited the highest charge-transfer resistance.

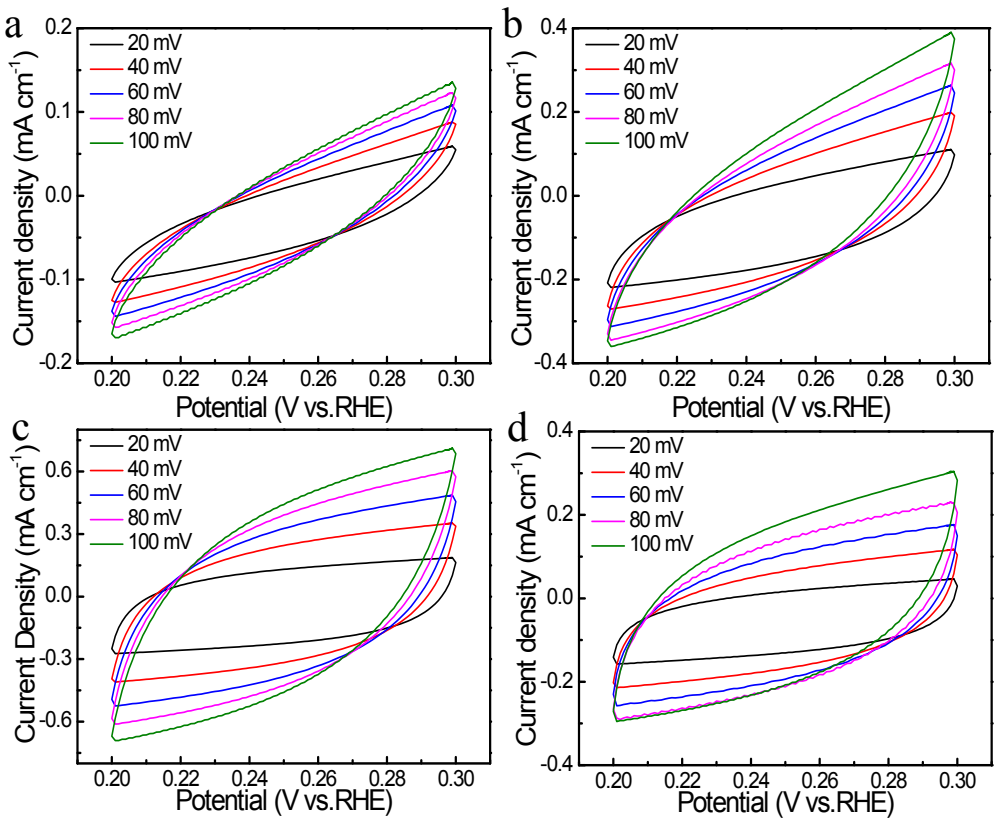

Figure S29. CV curves of (a) B/N-CNF-700, (b) B/N-CNF-800, (c) B/N-CNF, and (d) B/N-CNF-1000 at various scan rates (20 to 100 mV s^{-1}) in the range of 0.30 to 0.20 V. The electrochemical double layer capacitance of B/N-CNF was much higher than that of the B/N-CNF-700, B/N-CNF-800, and B/N-CNF-1000.

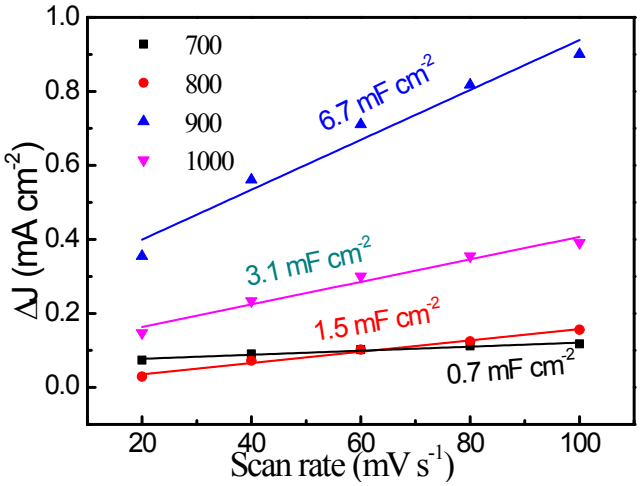

Figure S30. ECSA of B/N-CNF-700, B/N-CNF-800, B/N-CNF, and B/N-CNF-1000.

Table S1. Comparison of the NRR activity of MCHMs/CP to produce NH_3 with respect to that of other previously reported NRR electrocatalysts.

Catalyst	Electrolyte	FE (%)	NH_3 yield	Ref.
B/N-CNF	0.1 M KOH	13.2	20.0 μg h^{-1} mg^{-1}_{cat}	This work
Au nanorods	0.1 M KOH	3.9	1.6 μg h^{-1} cm^{-2}	1
α-Au/CeOx-RGO	0.1 M HCl	10.1	8.3 μg h^{-1} mg^{-1}_{cat}	2
Au/TiO_2	0.1 M HCl	8.1	21.4 μg h^{-1} mg^{-1}_{cat}	3
Ag-Au@ZIF	THF-based electrolyte	18	0.6 μg h^{-1} cm^{-2}	4
Pd/C	0.1M PBS	8.2	4.5 μg h^{-1} mg^{-1}_{cat}	5
Ru single-atom	0.05 M H_2SO_4	29.6	120.9 μg h^{-1} mg^{-1}_{cat}	6
TiO_2/Ti	0.1 M Na_2SO_4	2.5	9.2×10^{-11} mol s^{-1} cm^{-2}	7
TiO_2 NP-RGO	0.1 M Na_2SO_4	3.3	15.1 μg h^{-1} mg^{-1}_{cat}	8
Fe/Fe_3O_4	0.1M PBS	8.3	~0.2 μg h^{-1} cm^{-2}	9
γ-Fe_2O_3 nanoparticles-CNT	0.1 M KOH	1.9	0.2 μg h^{-1} mg^{-1}_{cat}	10
MoS_2/CC	0.1 M Na_2SO_4	1.2	4.9 μg h^{-1} cm^{-2}	11
MoN	0.1 M HCl	1.2	3.0×10^{-10} mo1 s^{-1} cm^{-2}	12
VN	0.1 M HCl	2.3	8.4×10^{-11} mol s^{-1} cm^{-2}	13
Ti_3C_2Tx Mxene	0.01 M HCl+Li_2SO_4	4.6	4.7 μg h^{-1} cm^{-2}	14
Nb_2O_5 nanofiber	0.1 M HCl	9.26	43.6 μg h^{-1} mg^{-1}_{cat}	15
N-doped porous carbon	0.05 M H_2SO_4	1.42	23.8 μg h^{-1} mg^{-1}_{cat}	16
N-doped carbon nanospikes	0.25 M $LiClO_4$	11.56	97.2 μg h^{-1} cm^{-2}	17
ZIF-derived carbon	0.1 M KOH	10.2	57.8 μg h^{-1} cm^{-2}	18
B doped graphene	0.05 M H_2SO_4	10.8	9.8 μg h^{-1} mg^{-1}_{cat}	19

FePc/C	0.1 M Na_2SO_4	10.5	138.0 μg h^{-1} mg^{-1}_{cat}	[20]
W_2N_3	0.1 M KOH	11.7	11.7 μg h^{-1} mg^{-1}_{cat}	[21]
Eex-COF/NC	0.1 M KOH	45.4	12.5 μg h^{-1} mg^{-1}_{cat}	[22]
FC	0.05 M H_2SO_4	12.1	6.9 μg h^{-1} cm^{-2}	[23]
TiC/C nanofibers	0.1 M HCl	5.8	14.1 μg h^{-1} mg^{-1}_{cat}	[24]
Fe-N/C-CNTs	0.1M KOH	9.3	34.8 μg h^{-1} mg^{-1}_{cat}	[25]

Table S2. Element compositions of B-CNFs, N/CNFs and B/N-CNFs samples prepared by different calcination temperatures from XPS results.

Sample	B at.%	C at.%	N at.%	O at.%
B/N-CNFs-700	8.7	61.5	19.9	9.9
B/N-CNFs-800	20.5	45.6	19.1	14.8
B/N-CNFs-900	29.9	34.1	27.6	8.4
B/N-CNFs-1000	33.1	27.2	23.8	15.9
B-CNF	13.2	65.1	7.7	14.0
N-CNF	0	87.6	7.9	4.5

Table S3. Element compositions of B/N-CNFs samples before and after NRR from XPS results.

Sample	B at.%	C at.%	N at.%	O at.%
B/N-CNFs	29.9	34.1	27.6	8.4
B/N-CNFs (after NRR)	28.2	35.9	28.0	7.9

References

1. D. Bao, Q. Zhang, F. L. Meng, H. X. Zhong, M. M. Shi, Y. Zhang, J. M. Yan, Q. Jiang and X. B. Zhang, *Adv. Mater.*, 2017, **29**, 1604799
2. S. J. Li, D. Bao, M. M. Shi, B. R. Wulan, J. M. Yan and Q. Jiang, *Adv. Mater.*, 2017, **29**, 1700001.
3. M. M. Shi, D. Bao, B. R. Wulan, Y. H. Li, Y. F. Zhang, J. M. Yan and Q. Jiang, *Adv. Mater.*, 2017, **29**, 1606550.
4. H. K. Lee, C. S. L. Koh, Y. H. Lee, C. Liu, I. Y. Phang, X. Han, C. K. Tsung and X. Y. Ling, *Sci adv.*, 2018, **4**, eaar3208.
5. J. Wang, L. Yu, L. Hu, G. Chen, H. Xin and X. Feng, *Nat. Commun.*, 2018, **9**, 1795.
6. Z. Geng, Y. Liu, X. Kong, P. Li, K. Li, Z. Liu, J. Du, M. Shu, R. Si and J. Zeng, *Adv. Mater.*, 2018, e1803498.
7. R. Zhang, X. Ren, X. Shi, F. Xie, B. Zheng, X. Guo and X. Sun, *ACS Appl. Mater. Interfaces*, 2018, **10**, 28251-28255.
8. X. Zhang, Q. Liu, X. Shi, A. M. Asiri, Y. Luo, X. Sun and T. Li, *J. Mater. Chem. A*, 2018, **6**, 17303-17306.
9. L. Hu, A. Khaniya, J. Wang, G. Chen, W. E. Kaden and X. Feng, *ACS Catal.*, 2018, **8**, 9312-9319.
10. S. Chen, S. Perathoner, C. Ampelli, C. Mebrahtu, D. Su and G. Centi, *Angew. Chem. Int. Ed. Engl.*, 2017, **56**, 2699-2703.
11. L. Zhang, X. Ji, X. Ren, Y. Ma, X. Shi, Z. Tian, A. M. Asiri, L. Chen, B. Tang and X. Sun, *Adv. Mater.*, 2018, **30**, 1800191.
12. L. Zhang, X. Ji, X. Ren, Y. Luo, X. Shi, A. M. Asiri, B. Zheng and X. Sun, *ACS Sustain. Chem Eng.*, 2018, **6**, 9550-9554.
13. X. Yang, J. Nash, J. Anibal, M. Dunwell, S. Kattel, E. Stavitski, K. Attenkofer, J. G. Chen, Y. Yan and B. Xu, *J. Am. Chem. Soc.*, 2018, **140**, 13387-13391.
14. Y. Luo, G.-F. Chen, L. Ding, X. Chen, L.-X. Ding and H. Wang, *Joule*, 2018, **3**, 279-289

15. J. Han, Z. Liu, Y. Ma, G. Cui, F. Xie, F. Wang, Y. Wu, S. Gao, Y. Xu and X. Sun, *Nano Energy*, 2018, **52**, 264-270.

16. Y. Liu, Y. Su, X. Quan, X. Fan, S. Chen, H. Yu, H. Zhao, Y. Zhang and J. Zhao, *ACS Catal.*, 2018, **8**, 1186-1191.

17. Y. Song, D. Johnson, R. Peng, D. K. Hensley, P. V. Bonnesen, L. Liang, J. Huang, F. Yang, F. Zhang, R. Qiao, A. P. Baddorf, T. J. Tschaplinski, N. L. Engle, M. C. Hatzell, Z. Wu, D. A. Cullen, H. M. Meyer, 3rd, B. G. Sumpter and A. J. Rondinone, *Sci. adv.*, 2018, **4**, e1700336.

18. S. Mukherjee, D. A. Cullen, S. Karakalos, K. Liu, H. Zhang, S. Zhao, H. Xu, K. L. More, G. Wang and G. Wu, *Nano Energy*, 2018, **48**, 217-226.

19. X. Yu, P. Han, Z. Wei, L. Huang, Z. Gu, S. Peng, J. Ma and G. Zheng, *Joule*, 2018, **2**, 1610-1622.

20. C. He, Z.-Y. Wu, L. Zhao, M. Ming, Y. Zhang, Y. Yi and J.-S. Hu, *ACS Catal.,* 2019, **9**, 7311-7317.

21. H. Jin, L. Li, X. Liu, C. Tang, W. Xu, S. Chen, L. Song, Y. Zheng and S. Z. Qiao, *Adv. Mater.,* 2019, **31**, 1902709.

22. S. Liu, M. Wang, T. Qian, H. Ji, J. Liu and C. Yan, *Nat. Commun.,* 2019, **10**, 1-9

23. D. Yuan, Z. Wei, P. Han, C. Yang, L. Huang, Z. Gu, Y. Ding, J. Ma and G. Zheng, *J. Mater. Chem. A*, 2019, **7**, 16979-16983.

24. G. Yu, H. Guo, W. Kong, T. Wang, Y. Luo, X. Shi, Abdullah M. Asiri, T. Li and X. Sun, *J. Mater. Chem. A*, 2019, **7**, 19657-19661.

25. Y. Wang, X. Cui, J. Zhao, G. Jia, L. Gu, Q. Zhang, L. Meng, Z. Shi, L. Zheng, C. Wang, Z. Zhang and W. Zheng, *ACS Catalysis*, 2018, **9**, 336-344.